

System-Level Comparison of Multimodal and In-Band mmWave Sensing for Beam Prediction in 6G ISAC

Abidemi Orimogunje*†, Hyunwoo Park†, Igbafe Orikumhi†, Sunwoo Kim†, Dejan Vukobratovic‡

* African Center of Excellence in Internet of Things, University of Rwanda, Rwanda

†Department of Electronic Engineering, Hanyang University, South Korea

‡Faculty of Technical Sciences, University of Novi Sad, Serbia.

Abstract—Integrated sensing and communication (ISAC) can reduce beam-training overhead in mmWave vehicle-to-infrastructure (V2I) links by enabling in-band sensing-based beam prediction, while exteroceptive sensors can further enhance the prediction accuracy. This work develops a system-level framework that evaluates camera, LiDAR, radar, GPS, and in-band mmWave power, both individually and in multimodal fusion using the DeepSense-6G Scenario-33 dataset. A latency-aware neural network composed of lightweight convolutional (CNN) and multilayer-perceptron (MLP) encoders predict a 64-beam index. We assess performance using Top-k accuracy alongside spectral-efficiency (SE) gap, signal-to-noise-ratio (SNR) gap, rate loss, and end-to-end latency. Results show that the mmWave power vector is a strong standalone predictor, and fusing exteroceptive sensors with it preserves high performance: mmWave alone and mmWave+LiDAR/GPS/Radar achieve 98% Top-5 accuracy, while mmWave+camera achieves 94% Top-5 accuracy. The proposed framework establishes calibrated baselines for 6G ISAC-assisted beam prediction in V2I systems.

Index Terms—Beam management, Beam prediction, ISAC, Multimodal sensing, 6G.

I. INTRODUCTION

Future sixth-generation (6G) systems are converging toward integrated sensing and communication (ISAC), where co-located sensors at the infrastructure continuously perceive the environment while sustaining high-rate links [1]. At mmWave/THz frequencies, narrow analog beams are essential for overcoming severe path loss and maintaining high signal-to-noise ratio (SNR) [2]–[4]. However, exhaustive beam sweeping and frequent retraining of such beams introduce latency and control overhead, particularly in vehicle-to-infrastructure (V2I) settings with fast dynamics and frequent line-of-sight (LoS)/non-LoS transitions [5], [6]. Leveraging exogenous sensing (from camera, radar etc.) to predict beams can reduce in-band training and accelerate link recovery, a direction validated on the real-world DeepSense-6G dataset and emerging ISAC prototypes [7]–[9].

Recent studies demonstrate that (i) vision-position fusion can reach high Top-3 accuracies with real mmWave data, significantly cutting beam-training overhead [10], (ii) position-only models with commercial Global Positioning System (GPS) achieve modest Top-1 but still deliver low power loss

Corresponding author: remero@hanyang.ac.kr. Co-Corresponding author: oigbafe2@hanyang.ac.kr

(rate loss) relative to the optimal beam, suggesting that accuracy alone is not a faithful system metric [11], (iii) improved modality encoders and pooler-style transformers can boost accuracy and reduce complexity [12], and (iv) geometry-aware pipelines using Light Detection and Ranging (LiDAR), and camera for 3D localization can directly steer beams and reduce search overhead [13], with digital-twin ray tracing emerging to make beam bursts obstacle-aware in real time [14].

Building on these insights, we present a complete, validated, and reproducible ISAC-assisted multimodal framework for beam prediction using DeepSense-6G Scenario-33 dataset. Our contributions are summarized as follows:

- 1) We compares individual sensing modalities (camera, LiDAR, radar, GPS and in-band mmWave power), their pairwise and multimodal fusions using not only Top-*k* accuracy but also spectral efficiency (SE), SNR, rate loss and end-to-end latency, thereby aligning model performance with actual communication behavior.
- 2) We treat the 64-dimensional mmWave receive power vector as a first-class ISAC sensing modality alongside camera, LiDAR, radar and GPS. Each sensor is encoded using compact CNN or MLP backbones and a transformer-based fusion module aggregates the embeddings to predict the receive-beam index.
- 3) On Scenario-33, we show that the mmWave power vector alone is a strong anchor modality, while fusing GPS or LiDAR provides consistent gains and camera/radar offer situational improvements. We quantify how small variations in Top-1 accuracy translate into substantial changes in rate loss and SNR gap.

Collectively, this work advances ISAC-assisted beam prediction by moving beyond accuracy-only comparisons and coupling beam-selection quality with SNR/SE performance and sensing-to-beamforming latency on real 60-GHz V2I measurements. The framework offers practical guidance and a reproducible baseline for future 6G ISAC deployment.

The rest of the paper is organized as follows. Section II details the system model. Section III describes the proposed multimodal architecture, fusion strategy, and training pipeline. Section IV presents experimental results and Section V concludes the paper.

II. SYSTEM MODEL

We consider a V2I ISAC setup with two units [15]. **Unit 1** (infrastructure) is a stationary receiver operating at 60 GHz, equipped with a $N_r=16$ -element phased array and a receive codebook of size $B=64$. Co-located sensors; an RGB camera, a 3D LiDAR, a frequency modulated continuous wave (FMCW) radar, and a GPS-RTK receiver observe the scene. **Unit 2** (mobile) is a transmitter with a single active antenna element. All sensors are time-aligned to the mmWave sweep at timestamp t .

A. Communication Model

At time t , the transmitter emits a complex symbol $x_t \in \mathbb{C}$. The $N_r \times 1$ array observation at Unit 1 is

$$\mathbf{y}_t = \mathbf{h}_t x_t + \mathbf{n}_t, \quad (1)$$

where $\mathbf{h}_t \in \mathbb{C}^{N_r}$ is the downlink channel seen at the receiver and $\mathbf{n}_t \sim \mathcal{CN}(\mathbf{0}, \sigma^2 \mathbf{I})$ is thermal noise. Applying the i th receive beam yields the scalar post-combiner output

$$z_{t,i} = \mathbf{w}_i^H \mathbf{y}_t, \quad (2)$$

and the corresponding received power measurement

$$p_{t,i} = |z_{t,i}|^2, \quad i = 1, \dots, 64. \quad (3)$$

Collecting all beams produces the power vector, $\mathbf{p}_t = [p_{t,1}, \dots, p_{t,64}]^\top \in \mathbb{R}_{\geq 0}^{64}$, which we treat as both a communication measurement and a sensing feature. The optimal beam index at time t is

$$b_t^* = \arg \max_{i \in \{1, \dots, 64\}} p_{t,i}. \quad (4)$$

With noise variance σ^2 , the instantaneous post-beamforming SNR and rate for a candidate beam i are

$$\text{SNR}_{t,i} = \frac{p_{t,i}}{\sigma^2}, \quad (5)$$

$$R_{t,i} = \log_2(1 + \text{SNR}_{t,i}), \quad (6)$$

and the oracle spectral efficiency is R_{t,b_t^*} . Throughout, we adopt the standard codebook-based beam selection abstraction used in multimodal beam prediction works. For a predicted index \hat{b}_t , the achievable rate is

$$R_{t,\hat{b}_t} = \log_2 \left(1 + \frac{p_{t,\hat{b}_t}}{\sigma^2} \right). \quad (7)$$

We define performance gaps that align model quality with system impact:

$$\text{SNR_gap}_t [\text{dB}] = 10 \log_{10} \left(\frac{\text{SNR}_{t,b_t^*}}{\text{SNR}_{t,\hat{b}_t}} \right) \quad (8)$$

$$\text{Rate_loss}_t = R_{t,b_t^*} - R_{t,\hat{b}_t}, \quad (9)$$

$$\text{SE_opt} = \mathbb{E}_t[R_{t,b_t^*}], \quad (10)$$

$$\text{SE_pred} = \mathbb{E}_t[R_{t,\hat{b}_t}] \quad (11)$$

and additionally report the average power-loss metric advocated for real-world assessment. Oracle SE is always an upper bound, i.e., $\text{SE_opt} \geq \text{SE_pred}$.

B. Sensing Model

At every synchronized timestamp, Unit 1 provides the fused sensing set

$$\mathcal{S}_t = \{ \mathbf{I}_t, L_t, \mathcal{R}_t, \mathbf{g}_t \}, \quad (12)$$

where \mathbf{I}_t , L_t , \mathcal{R}_t , \mathbf{g}_t , represent the camera image, point cloud from LiDAR, radar features, and GPS-based features respectively. Each element is summarized as follows.

1) RGB Camera

An RGB camera is co-located with the mmWave array, and we use the RGB stream $\mathbf{I}_t \in \mathbb{R}^{540 \times 960 \times 3}$ sampled at 30 fps. It provides semantic and geometric cues within the base station's field of view.

2) LiDAR

A rotating 3D LiDAR (100 m range, up to 20 Hz) returns a point cloud $L_t = \{ \mathbf{q}_\ell \}_{\ell=1}^{N_L} \subset \mathbb{R}^3$ (N_L is the number of points in the LiDAR sweep) sampling the environment with approximately uniform azimuth-elevation spacing. LiDAR contributes metrically accurate ranges to structures and moving obstacles, complementing the mmWave power vector by revealing potential blockages and reflecting surfaces that shape the multipath.

3) FMCW Radar

Each radar frame consists of complex samples with dimensions $(A \times S \times C)$ corresponding to the number of receiver antennas A , samples per chirp S , and chirps per frame C . After standard preprocessing, we form magnitude range-velocity (\mathbf{H}_{RV}) and range-angle (\mathbf{H}_{RA}) representations via 2D FFTs and use $\mathcal{R}_t = \{ \mathbf{H}_{\text{RA}}, \mathbf{H}_{\text{RV}} \}$ as radar features. Radar contributes Doppler and angular information that is resilient to illumination in weather conditions and complements camera-LiDAR for dynamic targets.

4) GPS-RTK

A GPS receiver provides a geodetic feature vector \mathbf{g}_t . In position-aided beam management [11], relative geometry derived from GPS can reduce beam training overhead when fused with visual and radar cues, though the raw GPS may exhibit non-Gaussian errors that impact direct beam classification.

5) mmWave Receive Power Vector

The 64-dimensional mmWave receive-power vector (\mathbf{p}_t) is included as an explicit sensing channel. It captures the instantaneous angular receive-power profile over the 64-beam codebook and is therefore highly informative for beam alignment in learned ISAC systems. Using \mathbf{p}_t as an input feature is consistent with recent multimodal formulations that fuse exteroceptive sensing with in-band radio signatures [16].

C. Problem Formulation

Let $\mathcal{B} = \{1, \dots, 64\}$ denote the receive-beam codebook and \mathcal{S}_t , the synchronized ISAC observation at time t . The oracle beam index is defined from the radio measurement as (4)

The goal is to learn a predictor \mathcal{M}_θ that maps multi-modal observations to a beam posterior $\pi_t = \mathcal{M}_\theta(\mathcal{S}_t; \mathbf{p}_t) \in \mathbb{R}^{|\mathcal{B}|}$ and outputs

$$\hat{b}_t = \arg \max_{i \in \mathcal{B}} \pi_{t,i}. \quad (13)$$

Beyond top- k classification, the problem is system-centric: we seek predictions that (i) maximize spectral efficiency,

$$\text{SE}_{\text{pred}} = \mathbb{E} \left[\log_2 \left(1 + \frac{p_{t,b_t}}{\sigma^2} \right) \right], \quad (14)$$

and (ii) minimize the SNR gap to the oracle,

$$\text{SNR_gap} = \mathbb{E} \left[10 \log_{10} \left(\frac{p_{t,b^*}}{p_{t,b_t}} \right) \right], \quad (15)$$

while maintaining high Top-K accuracy and low sensing-plus-inference latency. Formally, we learn θ to optimize a multi-objective criterion

$$\min_{\theta} \mathbb{E} \left[\underbrace{\text{CE}(b_t^*, \pi_t)}_{\text{beam classification}} + \lambda_{\text{gap}} \cdot \text{SNR_gap} + \lambda_{\tau} \cdot \tau_t \right], \quad (16)$$

where CE is cross-entropy, τ_t aggregates sensor and network inference latency, and $(\lambda_{\text{gap}}, \lambda_{\tau})$ trade-off accuracy, rate/SNR optimality, and latency. We evaluate \mathcal{M}_{θ} for individual modalities and their fusions to quantify accuracy, spectral-efficiency loss, SNR gap, and end-to-end latency under realistic hardware impairments.

III. PROPOSED METHOD

We develop a multimodal beam prediction network that estimates the receive-beam index \hat{b}_t from synchronized ISAC observations \mathcal{S}_t in the Scenario-33 V2I setting. The design follows three principles: (i) treat the in-band communication signal as an additional sensing stream by embedding the 64-dimensional mmWave power vector; (ii) extract modality-specific features using lightweight CNN/MLP encoders that map all sensors into a shared embedding dimension; and (iii) fuse these embeddings with a transformer-based fusion module that can flexibly operate with any subset of available modalities. The network is trained as a beam-classifier and evaluated with both accuracy and communication-centric metrics.

A. Data preparation and synchronization

Scenario-33 provides synchronized sample per index consisting of an RGB camera frame, a 64×1 mmWave receive power vector, LiDAR point cloud, radar frame, and GPS measurements. We first convert the raw logs into a compact indexed dataset. For each sample index, the preprocessing pipeline:

- converts the mmWave measurements into a 64-dimensional receive-power feature vector;
- extracts LiDAR measurements as XYZ point-cloud features and stores them in a compact representation;
- interprets the radar measurements as 2D radar-intensity maps for subsequent processing;
- associates each sample with its corresponding camera observation; and
- transforms the GPS measurements into per-sample feature vectors containing latitude, longitude, speed, and quality indicators.

All modalities are aligned by index, using the mmWave sequence as reference, and the aligned samples are split into train/validation/test using a contiguous 70/15/15 partition.

B. Modality-specific Encoders

Each sensor stream is embedded by a dedicated neural encoder that outputs a d -dimensional feature vector (with a shared embedding size $d=256$ in our implementation). This promotes symmetry across modalities and simplifies fusion.

1) mmWave power vector

The 64-dimensional mmWave receive power vector is encoded by a two-layer MLP. Concretely, the encoder applies a first linear layer from \mathbb{R}^{64} to \mathbb{R}^{2d} followed by a ReLU activation, and a second linear layer from \mathbb{R}^{2d} to \mathbb{R}^d followed by another ReLU. The resulting embedding $\mathbf{f}_t^{(\text{P}_t)} \in \mathbb{R}^d$ captures the angular power distribution across the receive codebook and serves as the communication-as-sensing feature.

2) Camera

For the RGB camera stream, we use a convolutional backbone that maps an image tensor $\mathbf{I}_t \in \mathbb{R}^{3 \times H \times W}$ to a d -dimensional embedding. We use a ResNet-18 model pre-trained on ImageNet and replace its classification head with a linear projection into \mathbb{R}^d . In addition, a lightweight CNN with ReLU activations is used. In both cases, the camera encoder outputs $\mathbf{f}_t^{(\text{I}_t)} \in \mathbb{R}^d$, which summarizes semantic and geometric context around the BS.

3) LiDAR

LiDAR point clouds are first converted into a bird's-eye-view (BEV) occupancy image on a fixed $(H_{\text{bev}}, W_{\text{bev}})$ grid over a pre-defined field of view. The resulting single-channel BEV map is fed to a encoder, which shares the same structure as the CNN backbone but with 1 input channel. This encoder applies stacked convolutions with ReLU and pooling followed by adaptive average pooling and a linear projection, yielding $\mathbf{f}_t^{(\text{L}_t)} \in \mathbb{R}^d$. This representation encodes road layout, static structures, and potential blockage geometry in a compact raster form.

4) Radar

Radar frames are loaded as real-valued 2D maps (after magnitude, dimensionality reduction, normalization, and resizing). These are passed to a CNN encoder, which is an architecture consisting of three convolutional layers with ReLU activations and intermediate pooling. This is followed by adaptive average pooling and a projection into \mathbb{R}^d . The radar encoder produces $\mathbf{f}_t^{(\mathcal{R}_t)} \in \mathbb{R}^d$, capturing range/angle structure and motion cues that are complementary to camera and LiDAR.

5) GPS-RTK

The features are represented as a fixed-length vector (e.g., latitude, and longitude) which are normalized. This vector is fed to an MLP encoder identical in form to the mmWave power encoder i.e., a two-layer ReLU MLP with an intermediate width of $2d$ and output dimension d . The GPS branch produces $\mathbf{f}_t^{(\text{g}_t)} \in \mathbb{R}^d$, providing coarse geometric information (relative position and motion) that helps disambiguate beams, especially when other modalities are degraded.

C. Transformer-based Multimodal Fusion

Let \mathcal{M}_t denote the set of modalities available at time t , and let $\mathcal{F}_t = \{\mathbf{f}_t^{(m)} : m \in \mathcal{M}_t\}$ be their embeddings. We fuse these modality embeddings using a token-based

transformer encoder. First, a modality projector maps the set of embeddings into a sequence of tokens. A learnable token is prepended to the sequence, and a fixed set of learned positional embeddings is added to encode token order. This yields a tensor where the tokens correspond to camera, LiDAR, radar, GPS, and/or mmWave embeddings, depending on which modalities are present. We then apply a multi-layer transformer encoder with multi-head self-attention over this token sequence. Because the token list is constructed only from modalities present in the batch, the same architecture can operate seamlessly with any subset of sensors (e.g., mmWave-only, camera+GPS, or full fusion).

D. Latency-aware evaluation

Although latency is not explicitly part of the training loss, the implementation tracks both sensor and inference latency during evaluation. For each batch, we measure the forward-pass time of the model and aggregate it across all samples to obtain an average inference latency. This is combined with user-specified per-modality sensor latencies to estimate end-to-end latency for a given sensor combination. Alongside Top- k accuracy, we compute spectral efficiency under the predicted and oracle beams, SNR gap in dB, and the gain ratio between predicted and optimal beam power. This evaluation protocol directly links multimodal perception quality to communication performance and timing constraints in the considered V2I ISAC setting.

IV. RESULTS AND DISCUSSION

A. Evaluation Metrics

We train and evaluate each sensor combination on DeepSense-6G Scenario-33 [15], using the receive-beam codebook \mathcal{B} . Besides Top- k accuracy, we report: (i) the average SNR gap (SNR_{gap} in dB) to the oracle beam (ii) the predicted vs. oracle spectral efficiencies (SE_{pred} and SE_{opt} in bps/Hz), (iii) the average rate loss ($\mathbb{E}[\Delta R]$) and (iv) the end-to-end latency. Hence, we present all metrics per sensor combination and compare them across combinations.

B. Overall Accuracy and Learning Behavior

Figure 1 shows training dynamics for principal sensing modality fusion. The per-modality curves in Figs. 2–6 underline complementary behaviors: GPS improves steadily as the model internalizes BS-UE geometry; LiDAR benefits from BEV pre-processing, yielding rapid early gains; camera and radar progress more gradually but contribute additional improvements once fused with geometry and mmWave.

The cross-combination comparison in Fig. 7 confirms that mmWave power is a strong single modality with high Top-3/Top-5 accuracy of approximately 93%/98%. Adding GPS or radar or LiDAR consistently maintains Top-1/3/5 accuracies with modest complexity as shown in Table I.

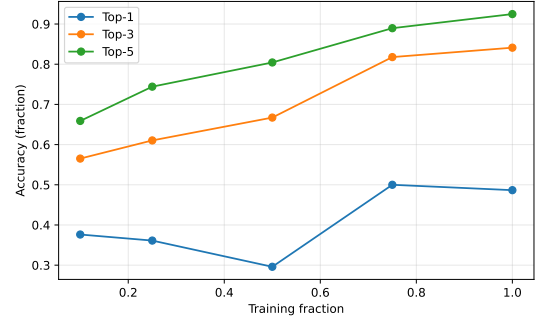


Fig. 1: Learning curves for principal modalities and their fusion (Top-1/3/5 accuracy vs. Dataset).

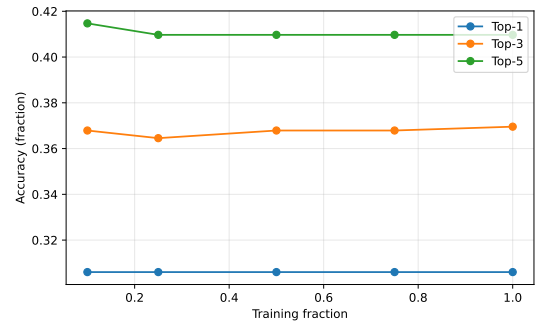


Fig. 2: Learning curve for LiDAR modality.

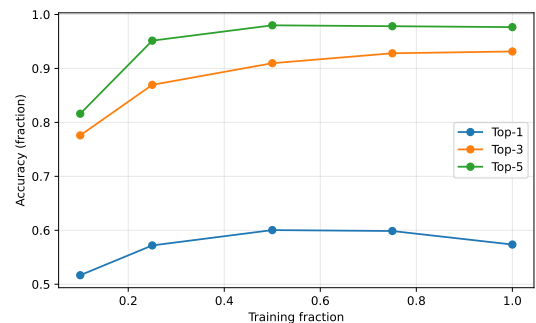


Fig. 3: Learning curve for mmWave power modality.

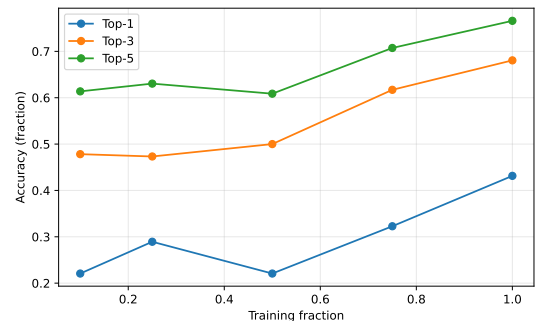


Fig. 4: Learning curve for Camera modality.

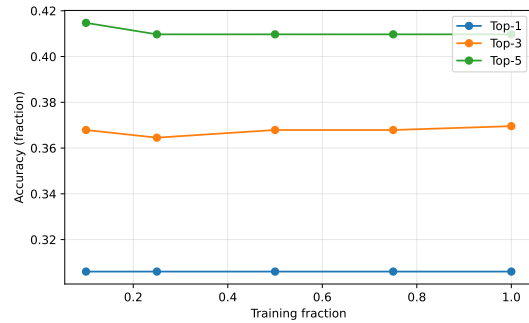


Fig. 5: Learning curve for GPS modality.

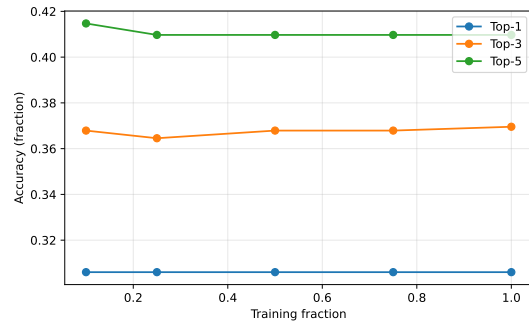


Fig. 6: Learning curve for Radar modality.

C. Spectral Efficiency and SNR Gap

Accuracy differences do not always translate linearly to communication quality. Figure 8 compares SE_{pred} to the oracle SE_{opt} . The mmWave-only baseline already attains a small SE gap on Scenario-33; fusing GPS (robust bearing/range cues) and LiDAR (blockage/reflector geometry) further compresses this gap, yielding disproportionately lower $\mathbb{E}[\Delta R]$ relative to the change in Top-1 accuracy. Figure 9 reports the average SNR gap as defined in Sec. II. The mmWave-only configuration exhibits a sub-dB average gap, and mmWave+GPS/LiDAR reduces this further. Camera and radar contribute in low-visibility or high-dynamics segments, with the largest net benefit observed in fusion alongside the mmWave/GPS/LiDAR trio.

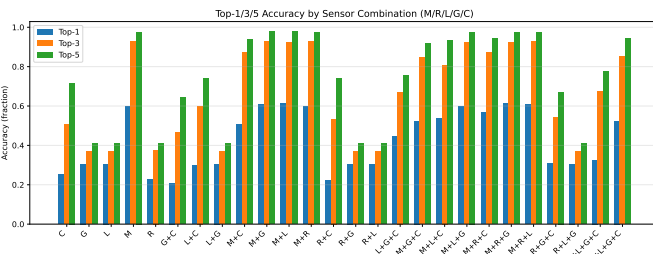


Fig. 7: Top-1/3/5 accuracy by sensor combination. Camera, GPS, LiDAR, mmWave and radar sensing modalities are represented with C, G, L, M and R respectively.

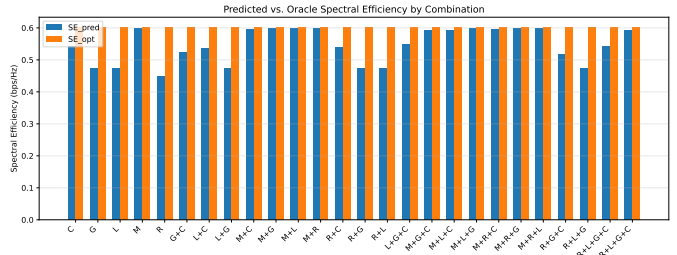


Fig. 8: SE_{pred} vs. SE_{opt} per combination. Geometry-aided fusion (mmWave+GPS/LiDAR) narrows the SE gap disproportionately to Top-1 changes.

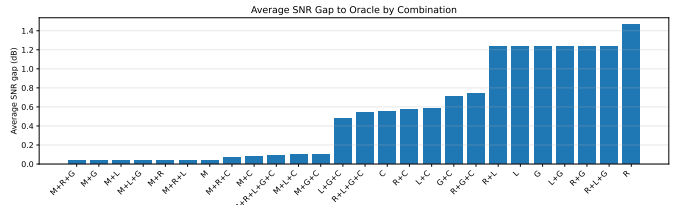


Fig. 9: Average SNR gap SNR_gap (in dB) to the oracle beam. mmWave-only is sub-dB on Scenario-33; GPS/LiDAR further reduce the gap; camera/radar add situational gains.

TABLE I: Performance of sensing modalities (alone and fused with mmWave) on Scenario-33.

| Sensing modality | Top-1 | Top-3 | Top-5 | $\mathbb{E}[\Delta R]$ | GR |
|--------------------------|-------|-------|-------|------------------------|------|
| <i>Single modality</i> | | | | | |
| mmWave | 0.60 | 0.93 | 0.98 | 0.0044 | 0.99 |
| GPS | 0.31 | 0.37 | 0.41 | 0.1306 | 0.77 |
| Radar | 0.23 | 0.38 | 0.41 | 0.1530 | 0.72 |
| LiDAR | 0.31 | 0.37 | 0.41 | 0.1306 | 0.77 |
| Camera | 0.25 | 0.51 | 0.72 | 0.0612 | 0.89 |
| <i>Fused with mmWave</i> | | | | | |
| mmWave+GPS | 0.61 | 0.93 | 0.98 | 0.0041 | 0.99 |
| mmWave+Radar | 0.60 | 0.93 | 0.98 | 0.0043 | 0.99 |
| mmWave+LiDAR | 0.61 | 0.92 | 0.98 | 0.0042 | 0.99 |
| mmWave+Camera | 0.51 | 0.87 | 0.94 | 0.0091 | 0.98 |
| M+G+L+C+R | 0.52 | 0.85 | 0.94 | 0.0102 | 0.98 |

Abbreviations: M = mmWave, G = GPS, L = LiDAR, C = Camera, R = Radar; $\mathbb{E}[\Delta R]$ = expected rate loss; GR = gain ratio.

D. Latency-Accuracy Trade-offs

Figure 10 decomposes end-to-end latency into sensing and inference components. The mmWave+GPS configuration is the most latency-efficient operating point, offering near-baseline SE_{pred} at minimal additional delay. LiDAR and radar increase sensing time yet can shrink the SNR gap in mobility and intermittent-blockage regimes. The camera branch adds semantic context at moderate overhead. Our multimodal fusion module (Sec. III) can operate with partial modality sets, allowing costly branches (e.g., camera) to be disabled when necessary while still preserving SE_{pred} through mmWave+GPS.

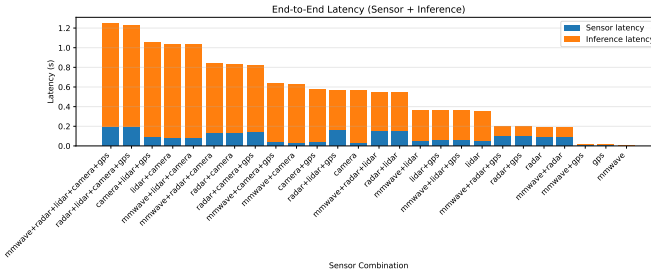


Fig. 10: Decomposition of end-to-end latency into sensing and inference components for different sensor configurations.

E. Data Efficiency and Ablations

Learning-curve slices (Figs. 2–6) indicate strong data efficiency. The mmWave and GPS models saturate rapidly, whereas LiDAR, camera, and radar continue to improve with additional training data, beginning to plateau in the intermediate-data regime. In the ablation study (Table I), we further observe that replacing a purely classification-oriented objective with the system-centric loss from Sec. II, which explicitly couples the learning signal to rate and SNR consistently lowers both Rate_loss and SNR_gap while preserving Top- k accuracy. This outcome better aligns the predictor with the system-level objectives defined earlier.

V. CONCLUSION

We presented a system-centric comparative analysis of ISAC beam prediction on DeepSense-6G Scenario-33. Our latency-aware fusion model treats the mmWave power vector as a sensing feature alongside camera, LiDAR, radar, and GPS, and is trained using a rate-aware loss. The results indicate that mmWave provides a strong anchor signal; GPS and LiDAR deliver consistent gains; and camera and radar offer situational improvements. Notably, even small changes in Top-1 accuracy can translate into meaningful reductions in spectral-efficiency and SNR gaps. Operationally, we recommend defaulting to mmWave+GPS and selectively enabling additional sensors under hardware constraints. Overall, the framework serves as a reproducible baseline that respects practical limitations and supports cross-scenario, temporal, and near-field extensions.

ACKNOWLEDGMENT

This work was jointly supported by the African Center of Excellence in Internet of Things (ACEIoT) University of Rwanda, Regional Scholarship and Innovation Fund (RSIF), and National Research Foundation of Korea under Grant RS-2024-00409492.

REFERENCES

- [1] D. Lee, Y. Lee, C. Song, J. Oh, N. T. Vi, and S. Cho, “A Survey on Integrated Sensing and Communication: Integrated System of RIS, UAV, Multiple Access,” in *2025 Internat. Conf. on Artificial Intell. in Informat. and Commun. (ICAIIIC)*, 2025, pp. 0028–0031.
- [2] J. Bang, H. Chung, J. Hong, H. Seo, J. Choi, and S. Kim, “Millimeter-Wave Communications: Recent Developments and Challenges of Hardware and Beam Management Algorithms,” *IEEE Commun. Mag.*, vol. 59, no. 8, pp. 86–92, 2021.
- [3] L. Li, W. Chen, Z. Chen, T. Hu, W. Mei, and B. Ning, “Enhancing Terahertz Communications Coverage with ISAC-Assisted Beam Management,” *IEEE Wireless Commun.*, vol. 31, no. 1, pp. 34–40, 2024.
- [4] H. Ahn, I. Orikumhi, J. Kang, H. Park, H. Jwa, J. Na, and S. Kim, “Machine Learning-Based Vision-Aided Beam Selection for mmWave Multiuser MISO System,” *IEEE Wireless Commun. Lett.*, vol. 11, no. 6, pp. 1263–1267, 2022.
- [5] W. Chen, L. Li, Z. Chen, Y. Liu, B. Ning, and T. Q. S. Quek, “ISAC-Enabled Beam Alignment for Terahertz Networks: Scheme Design and Coverage Analysis,” *IEEE Trans. Veh. Commun.*, vol. 73, no. 12, pp. 19 019–19 033, 2024.
- [6] H. Park, J. Kang, S. Lee, J. W. Choi, and S. Kim, “Deep Q-Network Based Beam Tracking for Mobile Millimeter-Wave Communications,” *IEEE Trans. Wireless Commun.*, vol. 22, no. 2, pp. 961–971, 2023.
- [7] K. Tan and C. Zhu, “Multimodal Sensing for Intelligent V2X: A Review of Recent Advances Toward Deployment,” *IEEE Internet Things J.*, vol. 12, no. 22, pp. 46 294–46 315, 2025.
- [8] C. Zheng, J. He, C. G. Kang, G. Cai, Z. Yu, and M. Debbah, “M2BeamLLM: Multimodal Sensing-empowered mmWave Beam Prediction with Large Language Models,” 2025. [Online]. Available: <https://arxiv.org/abs/2506.14532>
- [9] Y. Guo, W. Qin, Y. Xu, Y. Gu, C. Yin, and B. Xia, “Predictive Beam Tracking and Power Allocation With Cooperative Sensing for V2I Communication,” *IEEE Open J. of the Commun. Soci.*, vol. 5, pp. 6048–6063, 2024.
- [10] G. Charan, T. Osman, A. Hredzak, N. Thawdar, and A. Alkhateeb, “Vision-Position Multi-Modal Beam Prediction Using Real Millimeter Wave Datasets,” in *2022 IEEE Wireless Commun. and Netw. Conf. (WCNC)*, 2022, pp. 2727–2731.
- [11] J. Morais, A. Bchbodi, H. Pezeshki, and A. Alkhateeb, “Position-Aided Beam Prediction in the Real World: How Useful GPS Locations Actually are?” in *ICC 2023 - IEEE Internat. Conf. on Commun.*, 2023, pp. 1824–1829.
- [12] Y. Yeo, J. Kim, J. Kim, and J. Lee, “Multi-modal sensing-assisted beam prediction using real-world dataset,” *J. of Commun. and Netw.*, vol. 27, no. 5, pp. 412–419, 2025.
- [13] H. Kim, T. Roh, and B. Shim, “Multi-modal Sensing-aided Beam Management for 6G Communication Systems,” in *2024 IEEE 100th Veh. Technol. Conf. (VTC2024-Fall)*, 2024, pp. 1–5.
- [14] K. Heimann, J. An, L. Hito, S. Saidi, and C. Wietfeld, “Obstacle-Aware Proactive Beam Management Based on Real-Time Ray Tracing for mmWave Networks,” in *2025 IEEE 101st Veh. Technol. Conf. (VTC2025-Spring)*, 2025, pp. 1–5.
- [15] A. Alkhateeb, G. Charan, T. Osman, A. Hredzak, J. Morais, U. Demirhan, and N. Srinivas, “DeepSense 6G: A Large-Scale Real-World Multi-Modal Sensing and Communication Dataset,” *IEEE Commun. Mag.*, vol. 61, no. 9, pp. 122–128, 2023.
- [16] T. Kikuzuki, M. Boloursaz Mashhadi, Y. Ma, and R. Tafazolli, “Attention on the Preambles: Sensing With mmWave CSI,” *IEEE Open J. of the Commun. Soci.*, vol. 5, pp. 6430–6442, 2024.